



Cite this: *Phys. Chem. Chem. Phys.*, 2017, 19, 13341

Interconnected LiCuVO₄ networks with *in situ* Cu generation as high-performance lithium-ion battery anode†

Lei Wang,^{‡a} Yifan Dong,^{‡ab} Kangning Zhao,^{ab} Wen Luo,^a Shuo Li,^b Liang Zhou^{*a} and Liqiang Mai^{ib*ac}

Interconnected LiCuVO₄ networks were synthesized through a facile surfactant-assisted approach. Detailed investigations on the lithium storage mechanism manifest that metallic Cu nanoparticles are generated *in situ* during the first discharge process and remain mostly intact in the following cycles, thereby enhancing conductivity of the electrode. The interconnected networks with submicron sized primary particles endow the LiCuVO₄ with a large amount of active sites and thus high capacitive charge storage. Benefiting from a peculiar structure, the resultant interconnected LiCuVO₄ networks deliver extraordinary rate performance (216 mA h g⁻¹ up to 10 A g⁻¹) and ultralong cycling stability (~85% capacity retention after 5000 cycles at 5 A g⁻¹). The exceptional rate performance and cycling stability show that the interconnected LiCuVO₄ networks possess great potential for lithium-ion batteries.

Received 4th January 2017,
Accepted 17th March 2017

DOI: 10.1039/c7cp00049a

rs.c.li/pccp

Introduction

Nowadays, demands for innovative, environmental-friendly and sustainable energy sources have been continuously surging.^{1–5} Among the prevailing energy storage devices, rechargeable lithium-ion batteries (LIBs) are undoubtedly recognized as appealing candidates for hybrid electric vehicles (HEV), portable electronic devices as well as large-scale electric grids because of their intriguing properties of high energy efficiency, long lifespan, and environmental benignity.^{6–11} Nevertheless, a commercial graphite anode exhibits a relatively low theoretical capacity (372 mA h g⁻¹) and it suffers from potential safety issues of

lithium dendrite formation during deep or high-rate discharging, which limits widespread application of graphite in next-generation LIBs.^{12–15} Thus, it is of great significance to seek alternative anode materials possessing higher specific capacity, longer cycle life, and better safety to replace conventional graphite anodes.

Recently, it was found that some polyanionic compounds were capable of generating metallic components spontaneously during the discharge process, which could enhance their electronic conductivity and therefore electrochemical performance. For example, Chen¹⁶ *et al.* reported an Ag₂Mo₂O₇ anode for a sodium-ion battery. The metallic Ag extracted during the initial discharge spreads throughout the amorphous matrix and maintains unchanged, thus greatly reinforcing electronic conductivity. Zhao¹⁷ *et al.* proposed graphene oxide wrapped amorphous copper vanadate with *in situ* extraction of metallic Cu and its excellent electrochemical performances were ascribed to enhanced electronic conductivity. Kirshenbaum¹⁸ *et al.* designed a bimetallic material, Ag₂VP₂O₈, which formed a conductive silver matrix *in situ* during cathode reduction. This strategy brings the possibility of reducing the amounts of conductive additives in the future, which is quite promising. In this regard, the rational design of metal polyanionic compounds with *in situ* generation of a metallic component is highly desirable to achieve high conductivity and thus high power density.

As an important group of polyanionic compounds, metal vanadates have triggered extensive discussion because of their intriguing features and wide-spread applications in many fields.^{19,20} Among them, LiMVO₄ (M = Zn or Cu) compounds have attracted considerable attention owing to their merits such

^a State Key Laboratory of Advanced Technology for Materials Synthesis and Processing, Wuhan University of Technology, Wuhan 430070, Hubei, China.

E-mail: mlq518@whut.edu.cn, liangzhou@whut.edu.cn

^b Department of Chemistry, University of Wisconsin Madison, 1101 University Avenue, Madison, Wisconsin 53706, USA

^c Department of Chemistry, University of California, Berkeley, California 94720, USA

† Electronic supplementary information (ESI) available: The fabrication of I-LCVO; SEM images of LiCuVO₄ with different amounts of CTAB; TG curve of I-LCVO; SEM images of I-LCVO and A-LCVO before calcination; SEM, TEM and HRTEM images of A-LCVO; N₂ adsorption/desorption measurements and pore size distributions of I-LCVO and A-LCVO; CV and discharge/charge curves of A-LCVO; cycling performances of I-LCVO and A-LCVO at different current densities; cycling performance and discharge/charge curves of I-LCVO as full cell anode; *ex situ* TEM images and SAED patterns of I-LCVO at the first discharged and recharged states; *ex situ* SEM, TEM and EDS images of I-LCVO after cycling; CV curves of A-LCVO at various scan rates; ICP results of I-LCVO and A-LCVO. See DOI: 10.1039/c7cp00049a

‡ These authors contributed equally to this work.

as low cost, high theoretical capacity, and rich abundance.^{21–23} However, drawbacks of drastic volume variation and self-aggregation of bulk LiMVO₄ during charge/discharge processes may result in poor cycling performance, which hinders their application in LIBs.^{24,25} Fabricating nanostructured electrode materials has been proven to be an effective approach to provide sufficient accommodation to dramatic volume change and facilitate lithium ion diffusion.^{26–30} Besides, with generation of conductive metallic components, the overall electronic conductivity is enhanced, resulting in better kinetics. By this means, a high rate capability can be achieved.^{31–33} Thus, it is promising to design nanostructured LiMVO₄-based anode materials with conductive metallic component generation for high-performance LIBs.

Herein, we propose a facile surfactant-assisted route to synthesize interconnected LiCuVO₄ networks. The electrochemical mechanism, effects of nanoscale architecture, and *in situ* formed metallic Cu in electrochemical kinetics were investigated. During the first discharge process, conductive metallic Cu nanoparticles are generated, which is beneficial to decrease cell impedance and improve rate capability.¹⁸ Moreover, the interconnected LiCuVO₄ networks show typical pseudocapacitive behavior and enhanced capacitive contribution. Benefiting from a peculiar structure and enhanced capacitive contribution, the resultant well-designed interconnected LiCuVO₄ networks manifest exceptionally high-rate and long-cycle performances, making it a promising anode material for LIBs.

Experimental section

Materials preparation

Analytical grade NH₄VO₃, Li₂CO₃, Cu(NO₃)₂·3H₂O, hydrochloric acid, and cetyltrimethylammonium bromide (CTAB) were used as received without further treatment. In a typical synthesis, 1 mmol of NH₄VO₃ powder was dispersed in 40 mL deionized water under vigorous stirring at 80 °C. After that, 0.5 mmol of Li₂CO₃ and 1 mmol of Cu(NO₃)₂·3H₂O were added into the above suspension with continuous stirring. Then, 0.2 g of CTAB and 170 μL of concentrated hydrochloric acid solution (37 wt%) were added and stirred for 30 min. The mixture was kept in a water bath at 80 °C for 5 h and subsequently dried at 70 °C for 12 h in air. Finally, the solid was annealed at 500 °C for 6 h in air with a temperature ramping rate of 5 °C min⁻¹ and cooled to room temperature to obtain the target product.

Material characterization

X-ray diffraction (XRD) patterns were obtained with a Bruker D8 Discover X-ray diffractometer using Cu K α radiation ($\lambda = 1.5418 \text{ \AA}$). Scanning electron microscopy (SEM) images and energy dispersive X-ray spectra (EDS) were collected with a JEOL JSM-7100F microscope. Transmission electron microscopy (TEM) and high-resolution TEM (HRTEM) images associated with selected area electron diffraction (SAED) were recorded with a JEOL JEM-2100F microscope. Brunauer–Emmett–Teller (BET) surface areas were measured using a Tristar II 3020 instrument. X-ray

photoelectron spectroscopy (XPS) measurements and thermogravimetric analysis (TGA) were conducted using a VG MultiLab 2000 instrument and a STA-449C, respectively. An inductively coupled plasma mass spectrometer (ICP-MS, PerkinElmer Optima 2100DV) was used to determine the composition of the products.

Electrochemical measurement

The 2016 coin cells were assembled in a glove box filled with pure argon. Lithium foil was used as the counter electrode and reference electrode and a solution of LiPF₆ (1 M) in ethylene carbonate (EC)/dimethyl carbonate (DMC) (1:1 vol/vol) was used as the electrolyte. The working electrode was prepared by mixing the as-synthesized LiCuVO₄, acetylene black, and polyvinylidene fluoride (PVDF) in a weight ratio of 7:2:1. After coating onto copper foil, the electrode film was cut into ~0.5 cm² round slices, with a mass loading of 1.0–1.5 mg cm⁻². Galvanostatic charge/discharge measurements were performed in a potential window ranging from 0.01 to 3.0 V (*vs.* Li⁺/Li) using a multi-channel battery testing system (LAND CT2001A). Cyclic voltammetry (CV) and electrochemical impedance spectra (EIS) were obtained using electrochemical workstation (CHI 760D) and Autolab Potentiostat Galvanostat (PGSTAT302N), respectively. All the measurements were carried out at room temperature.

Results and discussion

The synthesis of interconnected LiCuVO₄ networks is schematically illustrated in Fig. S1 (ESI[†]). Hydrochloric acid, Li₂CO₃, Cu(NO₃)₂·3H₂O, and NH₄VO₃ are mixed with CTAB in the solution. The addition of CTAB plays its role efficiently in forming the homogeneous morphology and avoiding self-aggregation. During the water evaporation process, CTAB molecules adsorb on the surface of the as-obtained particles and constrain their overgrowth. Upon calcination, the CTAB molecules are burned-off, leaving behind unique interconnected LiCuVO₄ network (denoted as I-LCVO).³⁴ In this way, the crystallite size and morphology of the products are well-controlled. In contrast, in the absence of CTAB, the particles aggregate and overgrow, resulting in larger sizes, as well as uneven morphology, namely aggregated LiCuVO₄ (denoted as A-LCVO).

The XRD patterns of I-LCVO and A-LCVO are displayed in Fig. 1a. All the diffraction peaks can be well indexed to the orthorhombic LiCuVO₄ phase (JCPDS no. 00-018-0726, space group: *Imma*, $a = 5.6520 \text{ \AA}$, $b = 5.8100 \text{ \AA}$, $c = 8.7500 \text{ \AA}$, and $\alpha = \beta = \gamma = 90^\circ$). Thermogravimetric analysis (TGA) of I-LCVO conducted in air displays no obvious weight loss, indicating the complete removal of CTAB during calcination (Fig. S2, ESI[†]). To identify the elemental composition, ICP-MS was conducted, manifesting a Cu/V ratio of approximately 1:1 (Table S1, ESI[†]). Before calcination, both samples are composed of bulk particles, where no distinct difference can be detected, with an average diameter of 5 μm (Fig. S3, ESI[†]). After annealing, the A-LCVO shows an aggregated morphology with a rough surface, which may result from particle agglomeration (Fig. S4, ESI[†]). On the contrary, the as-prepared I-LCVO shows an interconnected network morphology (Fig. 1b and c), which is constructed

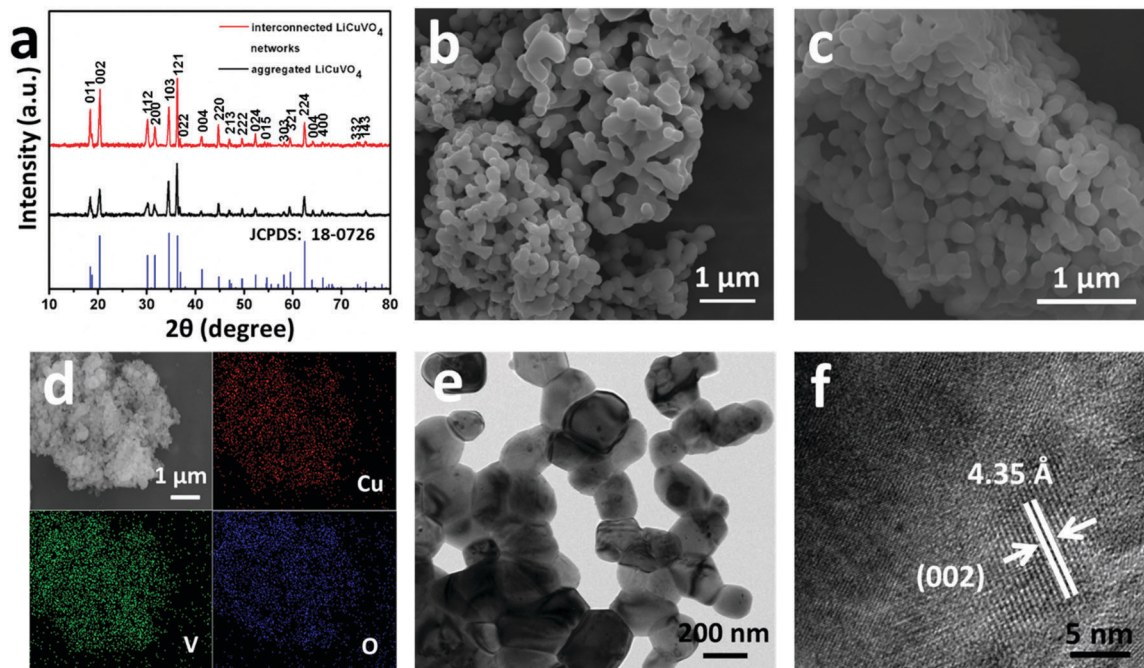


Fig. 1 (a) XRD patterns of the interconnected LiCuVO_4 network (I-LCVO) and the aggregated LiCuVO_4 (A-LCVO). (b and c) SEM images of I-LCVO. (d) EDS elemental mappings of I-LCVO. (e) TEM image of I-LCVO. (f) HRTEM image of I-LCVO.

by submicron sized primary particles with a size of ~ 150 nm. EDS element mapping results demonstrate the highly uniform distribution of copper, vanadium, and oxygen elements in I-LCVO (Fig. 1d). The morphology was further confirmed by TEM (Fig. 1e), in which interparticle macropores can be clearly observed in the I-LCVO network structure. The HRTEM image clearly reveals lattice fringes with a spacing of 4.35 Å, corresponding to the (002) facet of orthorhombic LiCuVO_4 (Fig. 1f). In addition, the N_2 sorption measurements (Fig. S5, ESI[†]) indicate that the BET surface area of the as-prepared I-LCVO (~ 13.0 m^2 g^{-1}) is much higher than that of A-LCVO (~ 5.8 m^2 g^{-1}). The Barrett-Joyner-Halenda (BJH) pore size distributions of I-LCVO and A-LCVO show the pores are centred at 40–50 nm for both samples.

The amount of CTAB was tuned from 0.1–0.8 g (Fig. S6, ESI[†]). The LiCuVO_4 sample prepared with a CTAB amount of 0.2 g displayed the most uniform and smallest size. When the CTAB amount was reduced to 0.1 g, irregular shaped bulk particles were obtained. When an excess amount of CTAB (0.4 g) was introduced, interconnected sub-micron particles with uneven size (500–1000 nm) were produced. Further increase of the CTAB amount to 0.8 g leads to interconnected microcrystals.

Coin-type cells were assembled to characterize the electrochemical performances of the products. CV curves of I-LCVO and A-LCVO were measured at a sweep rate of 0.1 mV s^{-1} in a voltage range from 0.01 to 3.0 V (*vs.* Li^+/Li) (Fig. 2a and Fig. S7a, ESI[†]). In general, the two samples possess quite similar CV profiles, indicating their identical electrochemical behavior. Besides, I-LCVO possesses larger CV areas than A-LCVO, implying a higher activity of I-LCVO. During the first cathodic sweep, three reduction peaks located near 1.86, 0.93, and 0.60 V

correspond to the decomposition of LiCuVO_4 (Cu^{2+} to metallic Cu), the insertion of lithium ions, and the formation of solid electrolyte interphase (SEI) layers, respectively.^{23,35,36} Meanwhile, an oxidation peak at ~ 1.37 V can be identified in the first anodic process, which may be attributed to the oxidation of V^{3+} to V^{4+} and V^{5+} . No anodic peaks for the oxidation of Cu^0 to Cu^{2+} was observed, which indicates that metallic copper nanoparticles generated during the first cathodic process are able to survive from the subsequent anodic process.²³ The following CV curves overlap quite well, demonstrating the highly reversible lithiation/de-lithiation processes. The discharge–charge voltage profiles for the 1st, 10th, 30th, and 50th cycles of I-LCVO and A-LCVO were collected at 0.1 A g^{-1} (Fig. 2b and Fig. S7b, ESI[†]). These two samples have very similar voltage profiles, but I-LCVO shows a better cycling performance. I-LCVO exhibits initial discharge capacity of 875 mA h g^{-1} at a current density of 0.1 A g^{-1} , with a Coulombic efficiency of $\sim 69\%$. From the second cycle, the capacity shows no obvious decay; a discharge capacity of 588 mA h g^{-1} is maintained after 50 cycles, demonstrating excellent cycling stability (Fig. 2c). The cycling performances of I-LCVO and A-LCVO at other current densities are compared in Fig. S8 (ESI[†]). No matter what the current density is, I-LCVO possesses higher capacity and better cyclability than A-LCVO. The Nyquist plots conducted before and after 10 cycles at 0.1 A g^{-1} (Fig. 2d) present a semicircle and a quasi-straight line, which are associated with the charge transfer resistance (R_{ct}) and the impedance of Li^+ diffusion in solid materials, respectively. Obviously, before cycling, the R_{ct} value of I-LCVO (297 Ω) is much lower than that of A-LCVO (410 Ω), indicating enhanced charge transfer kinetics of the I-LCVO. The R_{ct} values decrease significantly after cycling for both electrodes.

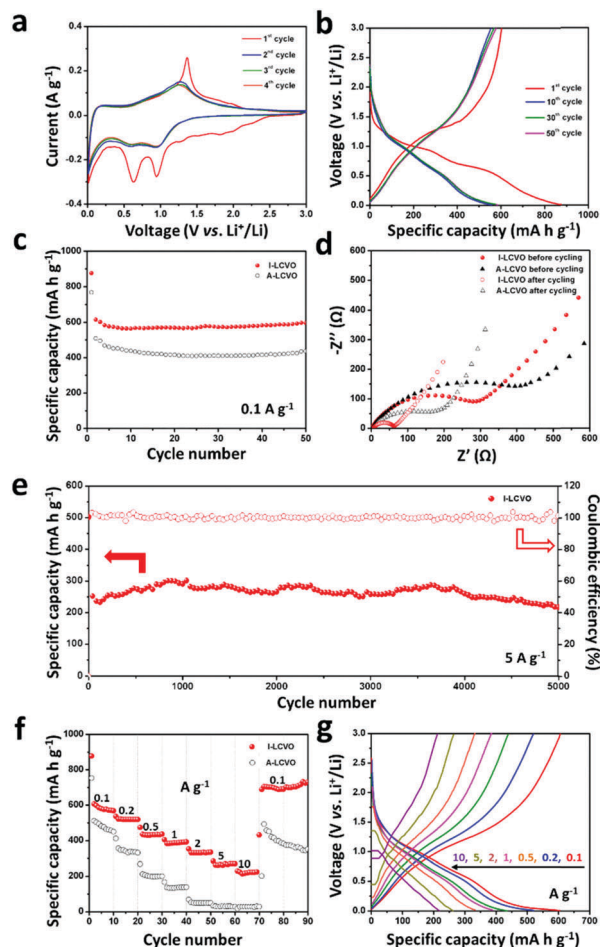


Fig. 2 (a) CV curves of I-LCVO at 0.1 mV s^{-1} . (b) Representative charge and discharge curves of I-LCVO at 0.1 A g^{-1} . (c) Cycling performances of I-LCVO and A-LCVO at 0.1 A g^{-1} . (d) Nyquist plots of I-LCVO before and after 10 cycles at 0.1 A g^{-1} . (e) Cycling performance and the corresponding Coulombic efficiency of I-LCVO at 5 A g^{-1} . (f) Rate performances of I-LCVO and A-LCVO. (g) Discharge/charge curves of I-LCVO at various current densities.

Besides high capacity, the I-LCVO also shows excellent cycling stability. It delivered a second discharge capacity of 253 mA h g^{-1} at 5 A g^{-1} . The capacity increases slightly from the 25th cycle to the 1000th cycle, which can be attributed to the lithiation induced activation.^{37–39} After 4000 cycles, the cycling curve shows a declining trend, which may result from deterioration in the crystal structure. After 5000 cycles, $\sim 85\%$ (214 mA h g^{-1}) of the second discharge capacity is maintained, demonstrating superior capacity retention after long-term cyclability (Fig. 2e). The rate performances of both I-LCVO and A-LCVO were tested within a range from 0.1 to 10 A g^{-1} . The I-LCVO exhibits average discharge capacities of $581, 519, 433, 388, 331, 265,$ and 216 mA h g^{-1} at current densities of $0.1, 0.2, 0.5, 1, 2, 5,$ and 10 A g^{-1} , respectively, which are significantly higher than those of A-LCVO. After the high-rate measurements, the current density returned to 0.1 A g^{-1} , and a capacity of 702 mA h g^{-1} is retrieved for I-LCVO, exhibiting remarkable rate recovery. This phenomenon of an increase in capacity may be

attributed to lithiation induced activation.^{37–39} Similar phenomena have been widely observed in transition metal oxides. In contrast, a capacity of merely 493 mA h g^{-1} is recovered for A-LCVO, and after the high rate test the capacity decays significantly with cycling (Fig. 2f). Representative galvanostatic discharge–charge voltage profiles of I-LCVO at different current densities of 0.1 to 10 A g^{-1} are depicted in Fig. 2g. The above results demonstrate the excellent high-rate capability and outstanding cyclability of these interconnected LiCuVO₄ networks. The excellent half-cell performance of the I-LCVO inspired us to further evaluate its feasibility in full cells. Lithium-ion full cells (LiCuVO₄||1 M LiPF₆/EC + DMC||LiFePO₄) based on an I-LCVO anode and commercial LiFePO₄ cathode were assembled. The detailed electrochemical behavior is shown in Fig. S9 (ESI[†]). The I-LCVO delivers a capacity of 161 mA h g^{-1} after 50 cycles at a current density of 1 A g^{-1} in the full cell, indicating the great cycling ability of I-LCVO in full cells.

Fig. 3 shows the *ex situ* XRD patterns of I-LCVO at the first discharged and charged states. When discharged to 0.01 V , most of the diffractions for LiCuVO₄ disappear. Meanwhile, the (111), (200), and (220) diffractions from metallic Cu and the (200), (002), and (320) diffractions from Li_{3+x}VO₄ appear. This demonstrates that LiCuVO₄ is first converted into metallic Cu and Li_{3+x}VO₄, and the latter is further lithiated into Li_{3+x}VO₄ during the first discharge. The (011) peak from LiCuVO₄ partially remains, suggesting the incomplete conversion of LiCuVO₄ to Cu and Li_{3+x}VO₄. When recharged to 3.0 V , the diffractions from Cu can be well maintained, demonstrating that *in situ* generated Cu can survive from the anodic process; and the Li_{3+x}VO₄ is de-lithiated into Li₃VO₄. This phenomenon

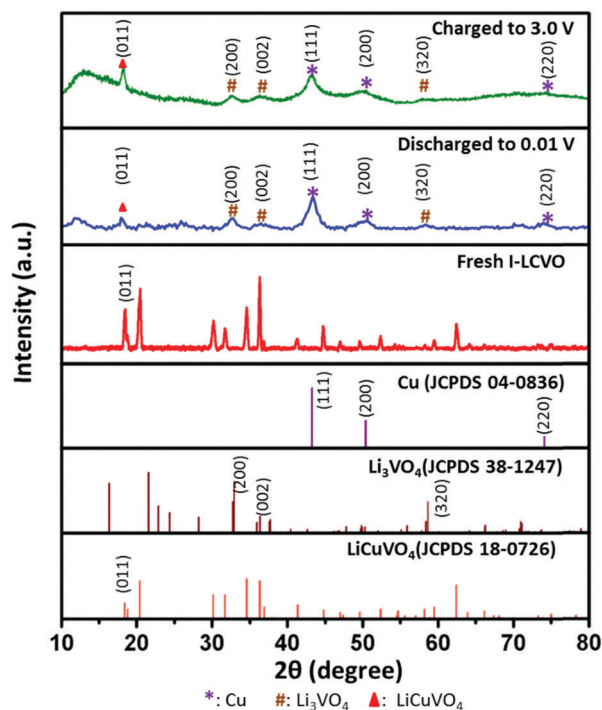


Fig. 3 *Ex situ* XRD patterns of the I-LCVO at the first discharged and charged states.

is consistent with a previous study.²³ No obvious change in XRD is detected due to their great similarity in structure.

The reaction mechanism of I-LCVO was further elucidated by *ex situ* XPS, TEM, and SAED. XPS measurements were provided to explore valence state changes of Cu and V. For pristine I-LCVO, the peaks located at 934.8 and 954.5 eV correspond to $\text{Cu}^{2+} 2p_{3/2}$ and $\text{Cu}^{2+} 2p_{1/2}$; the peak at 943.0 eV can be assigned to the satellite peak of $\text{Cu}^{2+} 2p_{3/2}$; and the peaks at 517.2 and 524.8 eV are indexed to $\text{V} 2p_{3/2}$ and $\text{V} 2p_{1/2}$ of V^{5+} . The XPS results suggest that the Cu and V exist as Cu^{2+} and V^{5+} in I-LCVO, respectively (Fig. 4a and b).^{40,41} The HRTEM image of pristine I-LCVO (Fig. S10a, ESI†) clearly reveals the (103) lattice fringes of orthorhombic LiCuVO_4 (2.59 Å). For the sample deeply discharged to 0.01 V, peaks for both Cu^0 and Cu^{2+} can be observed, and the intensity of Cu^0 is much higher than Cu^{2+} (Fig. 4c), which indicates the Cu mainly exists in the form of a metallic state after lithiation. The new peaks for Cu^0 appear at 952.6 eV ($\text{Cu}^0 2p_{1/2}$) and 933 eV ($\text{Cu}^0 2p_{3/2}$). The XPS peaks for $\text{V} 2p_{3/2}$ have three components at 517.2, 516.5, and 515.8 eV, corresponding to the V^{5+} , V^{4+} , and V^{3+} (Fig. 4d), respectively, which implies the reduction of V^{5+} to V^{4+} and consecutive reduction of V^{4+} to V^{3+} in the discharge process. In the *ex situ* HRTEM image of the discharged sample, lattice spacing of 2.08 Å can be assigned to the (111) facet of Cu (Fig. S10b, ESI†). Besides, (111) and (220) diffractions of Cu and (200) diffraction of $\text{Li}_{3+x}\text{VO}_4$ can be clearly observed in the SAED pattern of the discharged sample (Fig. S10d, ESI†).

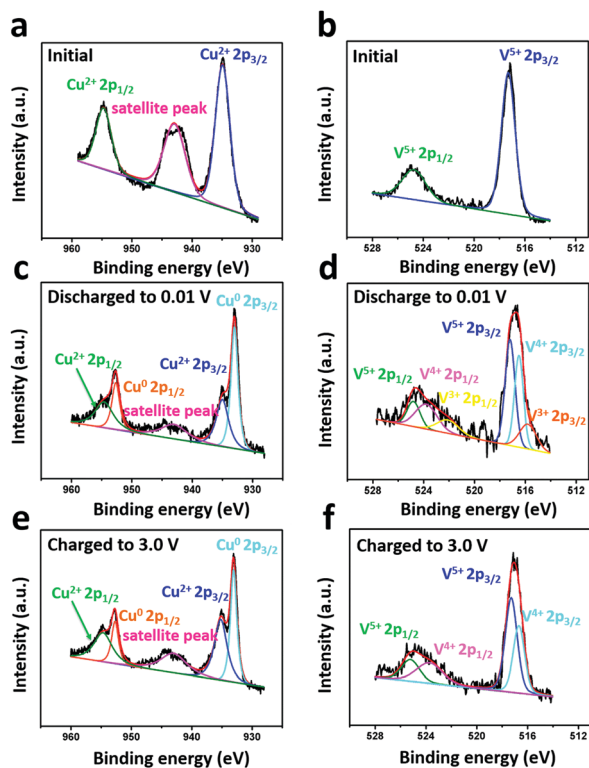


Fig. 4 XPS spectra of the (a and b) pristine I-LCVO, (c and d) I-LCVO in its discharged state, and (e and f) I-LCVO in its recharged state.

When the voltage returns to 3.0 V, most of the Cu still exists in its metallic form (Fig. 4e), which is in agreement with *ex situ* XRD result. As for the vanadium, it cannot be fully recovered to V^{5+} , so a considerable amount of V^{4+} still exist in the sample (Fig. 4f).^{40,41} In the *ex situ* HRTEM image (Fig. S10c, ESI†), the conductive metallic Cu nanoparticles can still be observed. In the SAED pattern, the (111) and (220) diffractions of Cu and (002) and (320) diffractions of Li_3VO_4 can be discerned (Fig. S10e, ESI†). The above *ex situ* XRD, XPS, TEM, and SAED results make it clear that the intrinsically generated Cu nanoparticles in the first discharge process are relatively stable and they are able to survive from subsequent recharge processes. A possible electrochemical mechanism of the LiCuVO_4 anode during cycling can be described as: $\text{LiCuVO}_4 + 2\text{Li}^+ + 2e^- \rightarrow \text{Li}_3\text{VO}_4 + \text{Cu}$; $\text{Li}_3\text{VO}_4 + x\text{Li}^+ + xe^- \leftrightarrow \text{Li}_{3+x}\text{VO}_4$.^{23,35,36} *Ex situ* SEM and TEM were conducted to investigate the morphological and structural changes. *Ex situ* SEM images reveal the interconnected network structure is well preserved after 10 cycles, implying its high mechanical flexibility to accommodate the volume change during cycling (Fig. S11(a and b), ESI†); *ex situ* TEM images show that the generated metallic Cu nanoparticles remain intact after 10 cycles (Fig. S11(c and d), ESI†). Besides, EDS element mapping results indicate that the vanadium, copper, and oxygen are uniformly distributed in the electrode after 5000 cycles (Fig. S11(e–h), ESI†).

To further explore the nature of the enhanced rate capability, electrochemical kinetics was investigated.^{42,43} CV curves of both I-LCVO and A-LCVO at various scan rates from 0.1 to 20 mV s^{-1} are shown in Fig. 5a and b, and Fig. S12 (ESI†). Generally, the CV curves display similar shapes and the redox peaks broaden gradually with an increase of sweeping rate. An analysis was carried out in regard to the peak current behavior *via* assuming a power-law relationship between the current (i) and the sweep rate (ν):^{44,45}

$$i = a\nu^b \quad (1)$$

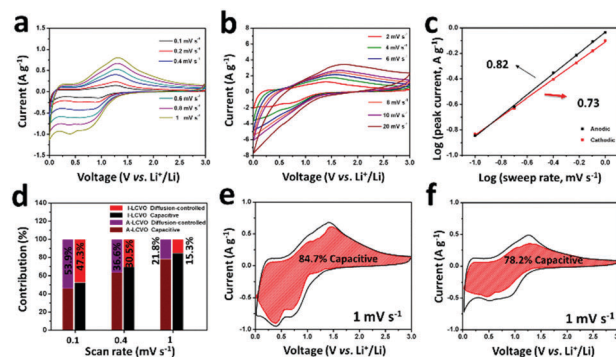


Fig. 5 The electrochemical kinetics of I-LCVO and A-LCVO. (a) CV curves of I-LCVO from 0.1 to 1 mV s^{-1} . (b) CV curves of I-LCVO from 2 to 20 mV s^{-1} . (c) Determination of the b -value of the anodic and cathodic peaks. (d) Capacitive and diffusion-controlled contributions of I-LCVO and A-LCVO at various scan rates. (e and f) The capacitive contributions of I-LCVO and A-LCVO at 1 mV s^{-1} .

The b -value in eqn (1) can be used to evaluate the charge storage form that occurs in the material. A b value of 0.5 expresses a total diffusion-controlled process, while a b value of 1 manifests a surface-controlled (capacitive) process. The slopes of $\log(i)$ versus $\log(\nu)$ gave b -values of 0.73 and 0.82 for the cathodic and anodic peaks, respectively (Fig. 5c). These b -values indicate the majority of the peak current is capacitive, suggesting the capacitive behavior dominates in the reaction of the interconnected LiCuVO₄ networks with fast kinetics.

The surface-controlled and diffusion-controlled contributions under a specific potential and sweep rate can be quantified by the analysis below, which was proposed by Dunn and coworkers:⁴⁶

$$i(V) = k_1\nu + k_2\nu^{1/2} \quad (2)$$

$k_1\nu$ corresponds to the capacitive contribution, and $k_2\nu^{1/2}$ stands for the diffusion-controlled contribution. By plotting $i(V)/\nu^{1/2}$ versus $\nu^{1/2}$, k_1 is determined as the slope; therefore, the capacitive and diffusion-controlled contributions can be obtained. Fig. 5d shows the contribution proportions for I-LCVO and A-LCVO at different scan rates. Generally, the capacitive contribution enhances gradually with an increase of sweeping rate. The capacity contributions of I-LCVO and A-LCVO at 1 mV s⁻¹ are shown in Fig. 5e and f. For both samples, the capacitive charge storage occupies a large proportion of the entire capacity. The capacitive contributions for I-LCVO and A-LCVO are ~84.7% and ~78.2%, respectively. The enhanced capacitive contribution and rate capability of I-LCVO can be ascribed to its unique interconnected network structure, which provides relatively large amounts of active sites and a large electrode/electrolyte contact area.

The b -values and predominantly capacitive proportion both confirm that the I-LCVO is dominated by the pseudocapacitive charge storage mechanism.⁴⁷ Based on the above analyses, the exceptional rate performance and lifetime extension of the interconnected LiCuVO₄ networks are probably attributed to individual structure features. On one hand, the interconnected LiCuVO₄ networks could provide sufficient tolerance for the dramatic volume change and facilitate lithium ions diffusion. The resultant predominant capacitive charge storage conversely endows the interconnected LiCuVO₄ networks with rapid discharge/charge capability. On the other hand, the intrinsically generated conductive copper nanoparticles during the first discharging are capable of decreasing cell impedance and enhancing electronic conductivity, thus further improving the electrochemical performance.

Conclusions

In this work, interconnected LiCuVO₄ networks were successfully fabricated through a facile surfactant-assisted method. The electrochemical mechanism of LiCuVO₄ was investigated. Metallic Cu nanoparticles are *in situ* generated during the first discharge process and remain mostly intact in following cycles, thereby enhancing conductivity of the electrode. The interconnected networks with submicron-sized primary particles endow the LiCuVO₄ with a large amount of active sites and thus high

capacitive charge storage. As an anode for LIBs, the interconnected LiCuVO₄ networks exhibited extraordinary rate performance (216 mA h g⁻¹ up to 10 A g⁻¹) and ultralong cycling stability (~85% remained even after 5000 cycles at 5 A g⁻¹). Such fantastic performances are ascribed to (i) the intrinsically generated conductive copper nanoparticles, which enhance the overall conductivity and (ii) the individual interconnected network structure, which provides enhanced capacitive charge storage. This work suggests that fabrication of electrode materials with an *in situ* generated metallic conductive component is promising for developing novel high performance electrodes for energy storage.

Acknowledgements

This work was supported by the National Key Research and Development Program of China (2016YFA0202603), the National Basic Research Program of China (2013CB934103), the National Natural Science Foundation of China (51521001, 21673171, 51502226), the National Natural Science Fund for Distinguished Young Scholars (51425204), and the Fundamental Research Funds for the Central Universities (WUT: 2016-JL-004, 2016III001, 2016III002). Prof. Dr Liqiang Mai gratefully acknowledged financial support from China Scholarship Council (No. 201606955096).

Notes and references

- 1 M. Armand and J.-M. Tarascon, *Nature*, 2008, **451**, 652.
- 2 A. Yoshino, *Angew. Chem., Int. Ed.*, 2012, **51**, 5798.
- 3 F. Cheng, J. Liang, Z. Tao and J. Chen, *Adv. Mater.*, 2011, **23**, 1695.
- 4 P. Simon, Y. Gogotsi and B. Dunn, *Science*, 2014, **343**, 1210.
- 5 H. Zhang, X. Yu and P. V. Braun, *Nat. Nanotechnol.*, 2011, **6**, 277.
- 6 R. Van Noorden, *Nature*, 2014, **507**, 26.
- 7 L. Mai, X. Tian, X. Xu, L. Chang and L. Xu, *Chem. Rev.*, 2014, **114**, 11828.
- 8 T. Sasaki, Y. Ukyo and P. Novák, *Nat. Mater.*, 2013, **12**, 569.
- 9 B. Dunn, H. Kamath and J.-M. Tarascon, *Science*, 2011, **334**, 928.
- 10 S. Chu and A. Majumdar, *Nature*, 2012, **488**, 294.
- 11 D. Larcher and J. Tarascon, *Nat. Chem.*, 2015, **7**, 19.
- 12 M. Ko, S. Chae, S. Jeong, P. Oh and J. Cho, *ACS Nano*, 2014, **8**, 8591.
- 13 Y. Yu, C. Niu, C. Han, K. Zhao, J. Meng, X. Xu, P. Zhang, L. Wang, Y. Wu and L. Mai, *Ind. Eng. Chem. Res.*, 2016, **55**, 2992.
- 14 B. Jang, M. Park, O. B. Chae, S. Park, Y. Kim, S. M. Oh, Y. Piao and T. Hyeon, *J. Am. Chem. Soc.*, 2012, **134**, 15010.
- 15 Z. Jian, M. Zheng, Y. Liang, X. Zhang, S. Gheyhani, Y. Lan, Y. Shi and Y. Yao, *Chem. Commun.*, 2015, **51**, 229.
- 16 N. Chen, Y. Gao, M. Zhang, X. Meng, C. Wang, Y. Wei, F. Du and G. Chen, *Chem. – Eur. J.*, 2016, **22**, 7248.
- 17 K. Zhao, F. Liu, C. Niu, W. Xu, Y. Dong, L. Zhang, S. Xie, M. Yan, Q. Wei and D. Zhao, *Adv. Sci.*, 2015, **2**, 1500154.

- 18 K. Kirshenbaum, D. C. Bock, C.-Y. Lee, Z. Zhong, K. J. Takeuchi, A. C. Marschilok and E. S. Takeuchi, *Science*, 2015, **347**, 149.
- 19 M. Xing, L.-B. Kong, M.-C. Liu, L.-Y. Liu, L. Kang and Y.-C. Luo, *J. Mater. Chem. A*, 2014, **2**, 18435.
- 20 G. Yang, H. Cui, G. Yang and C. Wang, *ACS Nano*, 2014, **8**, 4474.
- 21 F. Cheng and J. Chen, *J. Mater. Chem.*, 2011, **21**, 9841.
- 22 L. Zeng, X. Huang, C. Zheng, Q. Qian, Q. Chen and M. Wei, *Dalton Trans.*, 2015, **44**, 7967.
- 23 M. Li, X. Yang, C. Wang, N. Chen, F. Hu, X. Bie, Y. Wei, F. Du and G. Chen, *J. Mater. Chem. A*, 2015, **3**, 586.
- 24 J. Cabana, L. Monconduit, D. Larcher and M. R. Palacin, *Adv. Mater.*, 2010, **22**, E170.
- 25 M. Reddy, G. Subba Rao and B. Chowdari, *Chem. Rev.*, 2013, **113**, 5364.
- 26 P. G. Bruce, B. Scrosati and J. M. Tarascon, *Angew. Chem., Int. Ed.*, 2008, **47**, 2930.
- 27 C. Liu, F. Li, L. P. Ma and H. M. Cheng, *Adv. Mater.*, 2010, **22**, E28.
- 28 Q. Zhang, E. Uchaker, S. L. Candelaria and G. Cao, *Chem. Soc. Rev.*, 2013, **42**, 3127.
- 29 S. Lee, Y. Cho, H. K. Song, K. T. Lee and J. Cho, *Angew. Chem., Int. Ed.*, 2012, **51**, 8748.
- 30 S. H. Lee, S.-H. Yu, J. E. Lee, A. Jin, D. J. Lee, N. Lee, H. Jo, K. Shin, T.-Y. Ahn, Y.-W. Kim, H. Choe, Y.-E. Sung and T. Hyeon, *Nano Lett.*, 2013, **13**, 4249.
- 31 H.-S. Kim, J. B. Cook, S. H. Tolbert and B. Dunn, *J. Electrochem. Soc.*, 2015, **162**, A5083.
- 32 H. El-Shinawi, M. Böhm, T. Leichtweiß, K. Peppler and J. Janek, *Electrochem. Commun.*, 2013, **36**, 33.
- 33 Y. Dong, Y. S. Chui, R. Ma, C. Cao, H. Cheng, Y. Y. Li and J. A. Zapien, *J. Mater. Chem. A*, 2014, **2**, 13892.
- 34 X. Li, V. T. John, J. Zhan, G. He, J. He and L. Spinu, *Langmuir*, 2011, **27**, 6252.
- 35 R. Kanno, Y. Takeda, M. Hasegawa, Y. Kawamoto and O. Yamamoto, *J. Solid State Chem.*, 1991, **94**, 319.
- 36 X. Gao, J. Bao, G. Pan, H. Zhu, P. Huang, F. Wu and D. Song, *J. Phys. Chem. B*, 2004, **108**, 5547.
- 37 S. Grugeon, S. Laruelle, L. Dupont and J.-M. Tarascon, *Solid State Sci.*, 2003, **5**, 895.
- 38 Z. Cai, L. Xu, M. Yan, C. Han, L. He, K. M. Hercule, C. Niu, Z. Yuan, W. Xu and L. Qu, *Nano Lett.*, 2014, **15**, 738.
- 39 H. Sun, G. Xin, T. Hu, M. Yu, D. Shao, X. Sun and J. Lian, *Nat. Commun.*, 2014, **5**, 4526.
- 40 H. Ma, S. Zhang, W. Ji, Z. Tao and J. Chen, *J. Am. Chem. Soc.*, 2008, **130**, 5361.
- 41 F. Wu, S. Xiong, Y. Qian and S. H. Yu, *Angew. Chem., Int. Ed.*, 2015, **54**, 10787.
- 42 G. A. Muller, J. B. Cook, H.-S. Kim, S. H. Tolbert and B. Dunn, *Nano Lett.*, 2015, **15**, 1911.
- 43 D. Chao, C. Zhu, P. Yang, X. Xia, J. Liu, J. Wang, X. Fan, S. V. Savilov, J. Lin and H. J. Fan, *Nat. Commun.*, 2016, **7**, 12122.
- 44 T. Brezesinski, J. Wang, J. Polleux, B. Dunn and S. H. Tolbert, *J. Am. Chem. Soc.*, 2009, **131**, 1802.
- 45 Y. Zhu, L. Peng, D. Chen and G. Yu, *Nano Lett.*, 2015, **16**, 742.
- 46 V. Augustyn, P. Simon and B. Dunn, *Energy Environ. Sci.*, 2014, **7**, 1597.
- 47 L. Zhang, K. Zhao, Y. Luo, Y. Dong, W. Xu, M. Yan, W. Ren, L. Zhou, L. Qu and L. Mai, *ACS Appl. Mater. Interfaces*, 2016, **8**, 7139.